

## EDGE ARTICLE

[View Article Online](#)  
[View Journal](#) | [View Issue](#)



Cite this: *Chem. Sci.*, 2023, **14**, 613

All publication charges for this article have been paid for by the Royal Society of Chemistry

# Selective and high-rate CO<sub>2</sub> electroreduction by metal-doped covalent triazine frameworks: a computational and experimental hybrid approach<sup>†</sup>

Shintaro Kato, <sup>a</sup> Takuya Hashimoto, <sup>a</sup> Kazuyuki Iwase, <sup>b</sup> Takashi Harada, <sup>a</sup> Shuji Nakanishi <sup>\*ac</sup> and Kazuhide Kamiya <sup>\*ac</sup>

The electrochemical CO<sub>2</sub> reduction reaction (CO<sub>2</sub>RR) has attracted intensive attention as a technology to achieve a carbon-neutral society. The use of gas diffusion electrodes (GDEs) enables the realization of high-rate CO<sub>2</sub>RRs, which is one of the critical requirements for social implementation. Although both a high reaction rate and good selectivity are simultaneously required for electrocatalysts on GDEs, no systematic study of the relationship among active metal centers in electrocatalysts, reaction rate, and selectivity under high-rate CO<sub>2</sub>RR conditions has been reported. In the present study, we employed various metal-doped covalent triazine frameworks (M-CTFs) as platforms for CO<sub>2</sub> reduction reaction (CO<sub>2</sub>RR) electrocatalysts on GDEs and systematically investigated them to deduce sophisticated design principles using a combined computational and experimental approach. The Ni-CTF showed both high selectivity (faradaic efficiency (FE) > 98% at  $-0.5$  to  $-0.9$  V vs. reversible hydrogen electrode) and a high reaction rate (current density  $< -200$  mA cm<sup>-2</sup>) for CO production. By contrast, the Sn-CTF exhibited selective formic acid production, and the FE and partial current density reached 85% and 150 mA cm<sup>-2</sup>, respectively. These results for the CO<sub>2</sub>RR activity and selectivity at high current density with respect to metal centers correspond well with predictions based on first-principles calculations. This work is the first demonstration of a clear relationship between the computational adsorption energy of intermediates depending on metal species and the experimental high-rate gaseous CO<sub>2</sub>RR.

Received 6th July 2022  
Accepted 13th December 2022

DOI: 10.1039/d2sc03754h  
[rsc.li/chemical-science](http://rsc.li/chemical-science)

## Introduction

The excessive emission of CO<sub>2</sub> due to the use of fossil fuels is becoming a serious problem that threatens the sustainable development of society. The development of technologies that use CO<sub>2</sub> as an alternative carbon feedstock and convert it to other valuable chemicals is therefore important.<sup>1,2</sup> Various methodologies for effective CO<sub>2</sub> reduction have been widely investigated, including biological,<sup>3</sup> thermochemical,<sup>4</sup> photochemical,<sup>5</sup> and electrochemical approaches.<sup>1,2,6</sup> Among them, electrochemical CO<sub>2</sub> reduction has attracted intensive attention because it can be driven directly using electricity generated from renewable energy sources, such as solar and wind.<sup>7,8</sup> For

the industrial implementation of CO<sub>2</sub> electrolysis, the development of reaction systems that can rapidly and selectively reduce CO<sub>2</sub> to value-added products is critical.

Although dissolved CO<sub>2</sub> is conventionally used as the substrate, the current densities are limited to  $\sim 20$  mA cm<sup>-2</sup> because of the low solubility and slow diffusion of CO<sub>2</sub>.<sup>9,10</sup> The use of gas diffusion electrodes (GDEs) is one approach to overcome this problem originating from the low solubility and slow diffusion in the substrate.<sup>11-27</sup> Gaseous substrates can be directly supplied to the triple-phase boundary at the GDE, where the catalyst material, electrolyte, and gas pores intersect.<sup>10,28</sup> For example, de Arquer *et al.* achieved a current density of 1.3 A cm<sup>-2</sup> for ethylene formation at 45% energy efficiency using a GDE loaded with Cu nanoparticles,<sup>29</sup> and de Jesus and his coworkers achieved 600 mA cm<sup>-2</sup> for CO formation at a faradaic efficiency (FE) of 80% using a gas-fed zero-gap electrolyzer loaded with Ag nanocubes.<sup>30</sup> Based on the above reports, metal species in electrocatalysts are the most critical factor determining CO<sub>2</sub>RR activity. However, compared with the use of typical dissolved CO<sub>2</sub> as a substrate (*i.e.*, low-current-density electrolysis), the electrocatalytic activity for high-current-density CO<sub>2</sub> electrolysis depending on metal species has not

<sup>a</sup>Research Center for Solar Energy Chemistry, Graduate School of Engineering Science, Osaka University, 1-3 Machikaneyama, Toyonaka, Osaka 560-8531, Japan. E-mail: [nakanishi.shuji.es@osaka-u.ac.jp](mailto:nakanishi.shuji.es@osaka-u.ac.jp); [kamiya.kazuhide.es@osaka-u.ac.jp](mailto:kamiya.kazuhide.es@osaka-u.ac.jp)

<sup>b</sup>Institute of Multidisciplinary Research for Advanced Materials, Tohoku University, 2-1-1 Katahira, Aoba-ku, Sendai, Miyagi 980-8577, Japan

<sup>†</sup>Innovative Catalysis Science Division, Institute for Open and Transdisciplinary Research Initiatives, Osaka University, Suita, Osaka 565-0871, Japan

† Electronic supplementary information (ESI) available. See DOI: <https://doi.org/10.1039/d2sc03754h>



been well studied. Metal and metal oxide nanoparticles have different sizes and surface atomic arrangements depending on the metal species, even when synthesized using similar procedures.<sup>31–35</sup> Since immersion-type electrodes, including single-crystal or polycrystalline metal plates, are not available for GDEs, unlike in the case of conventional low-current-density electrolysis, the different morphologies of nanoparticles become the critical bottleneck for the systematic study of the dependence of gaseous CO<sub>2</sub> reduction activity on metal species.<sup>36,37</sup>

Recently, single-atom electrocatalysts (SAECs), which consist of singly isolated metal sites dispersed on heterogeneous supports, have drawn attention as a robust analog of homogeneous catalysts.<sup>38,39</sup> When well-designed materials are employed as supports for SAECs, the coordination environments of the metal centers are unambiguously defined, similar to the case for homogeneous organometallic catalysts.<sup>40,41</sup> Therefore, SAECs have great potential as alternatives to heterogeneous electrocatalysts composed of bulk metals. We have focused on metal-doped covalent triazine frameworks (M-CTFs) as a platform for SAECs on GDEs. CTFs are a class of conjugated microporous polymers with a 1,3,5-triazine moiety as the linker.<sup>42,43</sup> CTFs can immobilize a wide variety of 3d, 4d, and 5d metal centers due to abundant nitrogen atoms in their pores, and they exhibit various electrocatalytic functions corresponding to these metal centers, such as oxygen reduction and hydrogen oxidation reactions.<sup>44–55</sup> In particular, we have systematically examined the electrocatalytic CO<sub>2</sub>RR activity of CTFs doped with 3d metals (Co, Ni, or Cu) in neutral solutions using a conventional substrate of dissolved CO<sub>2</sub> at a total current density of 2 mA cm<sup>-2</sup>.<sup>48</sup> We observed that the adsorption strength of CO<sub>2</sub>RR intermediates for CO production varies depending on the metal center and that the CO generation activity corresponds to the adsorption strength. In addition, our group has recently demonstrated that gaseous ethylbenzene can be effectively oxidized to acetophenone in aqueous electrolytes using a GDE carrying a single-Ru-atom-doped CTF.<sup>11</sup> Given this background, we speculated that metal-doped CTFs (M-CTFs) would be an ideal platform for the electrocatalysts of gaseous substrates on GDEs. Furthermore, considering the availability of various metal atoms with a controlled structure, metal-doped CTFs are also suitable for theoretical studies to predict catalytic activity and gain atomic-level insights into the reaction mechanism.

Based on these considerations, CTFs doped with various metals are used as CO<sub>2</sub>RR electrocatalysts on GDEs, and we systematically investigate the relationship between metal species and high-rate CO<sub>2</sub>RR activity using a combined computational and experimental approach.

## Results and discussion

Our previous theoretical studies demonstrated that M-CTFs can widely tune the adsorption strength of intermediates for the dinitrogen<sup>56</sup> and oxygen reduction reactions<sup>57</sup> during electrochemical reactions when the metal species is varied. Similar to our approach in these previous studies, in the present work, we

attempted to predict the CO<sub>2</sub>RR activity and selectivity of M-CTFs by calculating the adsorption energy of CO<sub>2</sub>RR intermediates using density functional theory (DFT).

Let us consider the theoretical CO<sub>2</sub>RR on M-CTFs by calculating the Gibbs free energy of formation ( $\Delta G$ ) for each reaction

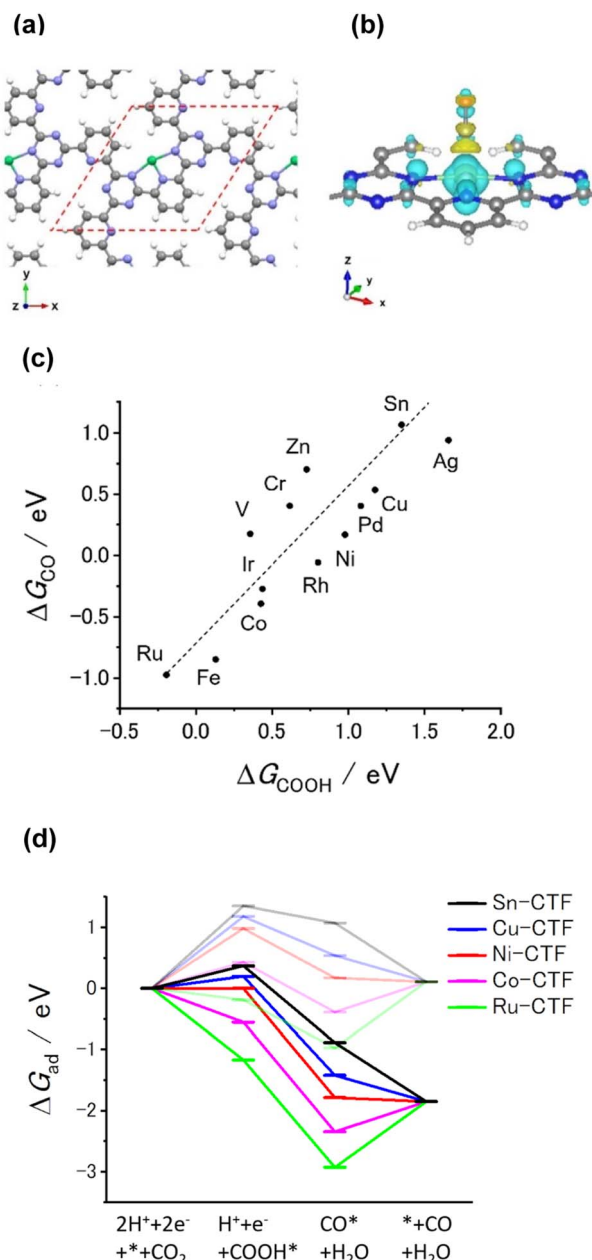


Fig. 1 (a) Optimized structure of Ni-CTF for DFT calculation (gray: C, white: H, blue: N, green: Ni). The red dashed line shows the unit cell. Approximately the same structure was obtained for all of the investigated M-CTFs. (b) Charge-density difference for Ni-CTF before and after COOH adsorption. The isosurface level is 0.003 e bohr<sup>-3</sup>. The yellow and cyan areas represent regions of electron accumulation and depletion, respectively (gray: C, white: H, blue: N, green: Ni). (c)  $\Delta G_{CO}$  expressed in terms of  $\Delta G_{COOH}$  for each M-CTF. (d) Free energy diagrams for CO generation on Sn (black), Cu (blue), Ni (red), Co (purple), and Ru (green)-doped CTFs at 0 V (pale lines) and  $-0.98$  V vs. CHE (dark lines).



intermediate  $\text{COOH}^*$  and  $\text{CO}^*$ . Fig. 1(a) and (b) show the relaxed structure and the difference in charge density on Ni-CTF before and after CO adsorption, respectively. An electron density accumulates at the p orbital of the adsorbed  $\text{CO}^*$ ; whereas a depletion in electron density is observed at the Ni site. These results indicate that p-back donation from the Ni site to  $\text{CO}^*$  occurred.<sup>58,59</sup> This electron transfer leads to effective activation of key intermediates.<sup>59</sup> Fig. 1(c) shows  $\Delta G(\text{CO})$  plotted against  $\Delta G(\text{COOH})$  for different M-CTFs. The linear relationship between  $\Delta G(\text{COOH})$  and  $\Delta G(\text{CO})$  indicates that the so-called scaling relationship applies to  $\text{CO}_2\text{RR}$  on SAECS.<sup>60–66</sup> That is,  $\Delta G(\text{COOH})$  and  $\Delta G(\text{CO})$  cannot be independently modulated.<sup>61–66</sup> On the basis of this relationship, a volcano-type relation accompanied by a single peak between  $\Delta G(\text{COOH})$  or  $\Delta G(\text{CO})$  and  $\text{CO}_2\text{RR}$  activity would appear despite the existence of more than one intermediate.<sup>67,68</sup> Both the  $\Delta G(\text{COOH})$  and the  $\Delta G(\text{CO})$  values indicate stronger adsorption on metal centers with fewer d-electrons.<sup>68–71</sup> When CO or COOH is adsorbed onto a metal center, bonding and antibonding orbitals are formed.<sup>68,69</sup> The degree of filling of the antibonding orbitals increases with increasing number of d-electrons, resulting in weaker adsorption of CO or COOH.<sup>68–71</sup> Fig. 1(d) shows the free energy diagram for CO production at 0 V and  $-0.98$  V vs. computational hydrogen electrode (CHE) on different M-CTFs ( $M = \text{Co, Cu, Ni, Ru, Sn}$ ). At  $-0.98$  V vs. CHE, the Sn- and Cu-CTFs exhibit an endergonic reaction for  $\text{COOH}^*$  formation, whereas a potential barrier exists at the CO desorption step for the Ru- and Co-CTFs (Fig. 1(d) and Table S1†). By contrast, all of the elementary steps on the Ni-CTF are exergonic. The dependence of the free energy diagrams on the metal centers can be explained as follows. The CO and COOH adsorption strength simultaneously increases with decreasing number of d-electrons (Fig. 1(c)). The  $\Delta G$  value for  $\text{COOH}^*$  formation decreases with increasing adsorption strength of  $\text{COOH}^*$ , whereas the barrier of CO desorption steps increases with increasing CO adsorption energy. Therefore, the Cu- and Sn-CTFs exhibited lower adsorption strengths than an optimal catalyst, resulting in a barrier for  $\text{COOH}^*$  formation. By contrast, the CO desorption step becomes the potential-determining step for the Ru- and Co-CTFs, whose adsorption strengths are greater than the optimal value. We also calculated the H-adsorption energies to evaluate the selectivity of  $\text{CO}_2\text{RR}$  vs. hydrogen evolution reaction (HER) (Fig. 2). There is a linear relationship between  $\Delta G(\text{H})$  and  $\Delta G(\text{COOH})$  in a similar manner to bulk metals and other SAECS.<sup>72–74</sup> When this linear relationship is applicable, stronger and weaker adsorption of  $\text{H}^*$  or  $\text{COOH}^*$  leads to the selectivity for HER and  $\text{CO}_2\text{RR}$ , respectively, based on previous reports.<sup>75,76</sup> These results made us predict that Fe- and Ru-CTFs might be active for the HER rather than  $\text{CO}_2\text{RR}$ .

$\text{HCOOH}$  is the other two-electron reduction product of  $\text{CO}_2$ .<sup>77–82</sup> Next, let us predict the selectivity of CO and  $\text{HCOOH}$  based on the DFT calculations. As shown in Fig. 1(c), 2, and S1,† there is a linear relationship between  $\Delta G(\text{COOH})$ ,  $\Delta G(\text{CO})$ , and  $\Delta G(\text{H})$ . In this case,  $\Delta G(\text{COOH})$ ,  $\Delta G(\text{CO})$ , and  $\Delta G(\text{H})$  can serve as the descriptor of the selectivity not only for  $\text{CO}_2\text{RR}$  against HER but for CO vs.  $\text{HCOOH}$  formation. When the adsorption of these

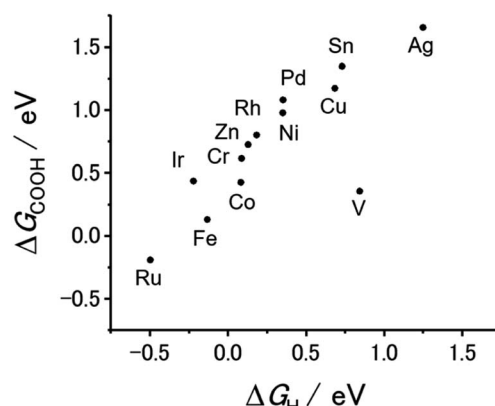


Fig. 2  $\Delta G_{\text{COOH}}$  expressed in terms of  $\Delta G_{\text{H}}$  for each M-CTF.

reactive species becomes weak (*i.e.*,  $\Delta G$  values shift to the positive side), a major product gradually changes  $\text{H}_2$  to CO, and then to  $\text{HCOOH}$ . We must note that reactive species for which adsorption energy serves as a descriptor are not necessarily reaction intermediates, which means this prediction does not suggest  $\text{COOH}^*$ ,  $\text{H}^*$  or  $\text{CO}^*$  is the intermediate for  $\text{HCOOH}$  production. In many reports, the key intermediates in the production of CO and  $\text{HCOOH}$  are  $\text{COOH}^*$  and  $\text{OCHO}^*$ , respectively.<sup>79–82</sup> The surface with a high affinity to COOH or H facilitates CO or  $\text{H}_2$  evolution, respectively. Therefore, the large negative potential needed for  $\text{HCOOH}$  production can be applied without CO and  $\text{H}_2$  formation only when the binding energy of both COOH and H (and CO) is weak,<sup>72,76</sup> which is the reason why we can utilize  $\Delta G(\text{COOH})$ ,  $\Delta G(\text{CO})$  or  $\Delta G(\text{H})$  as the descriptor for the selectivity. Based on this classification, we expected that CO and  $\text{HCOOH}$  become the main products on M-CTFs with moderate  $\Delta G$  (Ni-, Cu-, and Co-CTFs) and those with high  $\Delta G$  (Sn-CTF), respectively. Among them, the highest  $\Delta G$  for Ag-CTF does not correspond with the trend of reported SAECS.<sup>63,74,82</sup> The stability test of single atom sites using DFT calculations revealed that Ag-CTF exhibited the lowest stability of single atoms in M-CTF (for the detail, see Table S2† and its caption); there might be some inconsistency between the genuine and model structures for Ag-CTF. Thus, the experimental results for Ag-CTF are shown as the reference data in Fig. S2,† and we need further studies to clarify the reason for this mismatch.

We next attempted to experimentally determine the  $\text{CO}_2\text{RR}$  activity for the M-CTF/GDEs. The CTF was synthesized by polymerizing 2,6-dicyanopyridine in molten  $\text{ZnCl}_2$  containing carbon nanoparticles. The resultant CTF was impregnated with various metal chloride or acetate solutions to obtain M-CTFs ( $M = \text{Ag, Co, Cu, Ni, Fe, Ru, Sn}$ ). Details of the synthesis conditions are provided in the ESI.†

Table S3† lists the surface elemental composition for the M-CTF/GDEs, which was measured by X-ray photoelectron spectroscopy (XPS). The metal amounts in the M-CTF/GDEs are between 0.09 and 0.32 at%. Detailed characterization results for the powder forms of the Ni-, Cu-, and Co-CTFs are provided in our previous reports.<sup>48,83</sup> The XPS and X-ray absorption fine



structure (XAFS) results for these M-CTFs deposited onto GDEs are shown in Fig. 3(a) and S3–S5,† respectively. The results are basically consistent with those for the corresponding powder samples. The curve fitting of EXAFS spectra for Ni-CTF was conducted (Fig. S6† and Table S4†). Notably, the coordination numbers (CNs) of Ni-CTF was 3.4, which is smaller than that of 5,10,15,20-tetraphenyl-21*H*,23*H*-porphine Ni [Ni-TPP, *i.e.*, Ni-N<sub>4</sub> macrocycle]. This result corresponds to the previous results and suggest that M-CTF possess M–N<sub>3</sub> structure.<sup>48</sup>

The present paper describes the detailed properties of Sn-CTFs. Fig. S3 and S4(b)† show XPS and X-ray absorption near edge structure (XANES) spectra, respectively, of the Sn-CTF/GDE. The narrow XPS spectrum shows the Sn 3d<sub>5/2</sub> peak at 487 eV, which indicates that Sn<sup>IV</sup> was dominant in the Sn-CTF/GDE;<sup>84</sup> this interpretation was confirmed by the XANES spectra (for details, see the ESI†). Extended X-ray absorption fine structure (EXAFS) spectra for the Sn- and Ni-CTFs are shown in Fig. 3(a) and S5,† respectively. In the Fourier transformation of the *k*<sub>3</sub>-weighted EXAFS oscillations for the Sn-CTF (Fig. 3(a)), peaks corresponding to Sn–Sn bonds (2.9 Å) in Sn particles and Sn–O–Sn bonds (3.3 Å) in SnO<sub>2</sub> were not observed. High-resolution energy-dispersive X-ray (HR-EDX) mapping and high-angle annular dark-field scanning transmission electron microscopy (HAADF-STEM) images of the Sn-CTF are shown in Fig. 3(b) and S7,† respectively. Fig. 3(b) shows Sn atoms as small white spots (smaller than 0.5 nm). These results indicate that the Sn<sup>IV</sup> atoms were singly isolated in the as-prepared Sn-CTF. Scanning electron microscopy (SEM) images of cross-sections of the Ni-CTF/GDE are shown in Fig. 3(c) and S8.† The 50 nm catalyst particles were pasted onto a microporous layer composed of carbon nanoparticles. The thickness of the catalyst layers was ~30 μm. The SEM observations showed no specific

characteristics that depended on the metal species in the M-CTF/GDEs.

We analyzed the products of the CO<sub>2</sub>RR conducted in the presence of the M-CTF/GDEs. As shown in Fig. S9,† the M-CTF/GDEs enabled high-rate electrolysis at a current density greater than  $-100 \text{ mA cm}^{-2}$ . Fig. 4(a), (b) and S10† show the breakdown of the CO<sub>2</sub> reduction products of the M-CTFs under a constant potential of  $-0.9 \text{ V}$  *vs.* reversible hydrogen electrode (RHE) in 1 M KHCO<sub>3</sub>(aq) (pH 8.6). Only H<sub>2</sub>, CO, and HCOOH were detected on all the M-CTF/GDEs, and no further reduction products were observed (Fig. S11 and S12†). The Ni- and Co-CTFs produced CO as the main product of the CO<sub>2</sub>RR, whereas HCOOH was mainly generated on the Sn-CTF, consistent with the predictions based on DFT calculations (Fig. 2). In contrast, the HER, which competes with the CO<sub>2</sub>RR, was the main reaction for the Ru- and Fe-CTFs. The FE for CO reached greater than 98% for the Ni-CTF/GDE. However, the FE for HCOOH was 80% for the Sn-CTF/GDE. These results indicate that the selectivity of the CO<sub>2</sub>RR strongly depends on the metal species of the M-CTF. In the case of the Ni- and Sn-CTFs, we conducted XAFS characterizations after electrolysis to identify the active sites for high-rate CO<sub>2</sub>RR (Fig. S13†). The Fourier transformed EXAFS (FT-EXAFS) spectra of the M-CTF/GDEs after electrolysis still showed no obvious peaks corresponding to M–M and M–O–M bonds attributed to metal particles and oxides, respectively. These results indicate that the active sites for high-rate CO<sub>2</sub>RR were single metal atoms coordinated to CTFs.

We next investigated the potential window and the current density for the CO<sub>2</sub>RR on the Ni- and Sn-CTF/GDEs. Fig. 5(a) and (b) show the potential dependence of the FE and the partial current densities on the Ni-CTF/GDE, respectively. The FE for

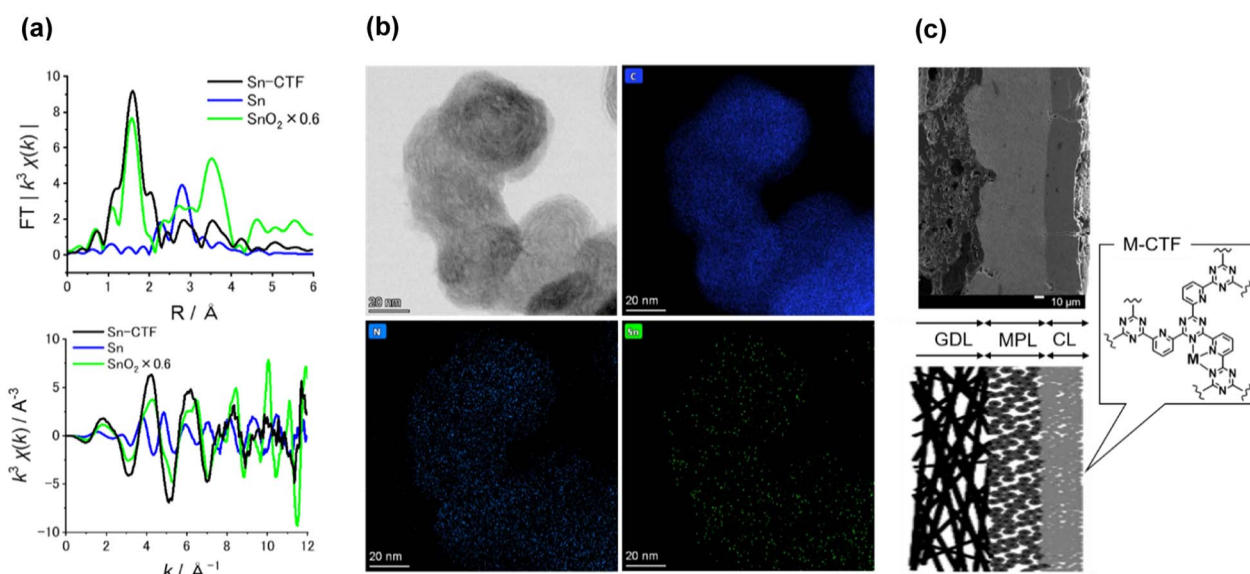


Fig. 3 (a) (upper)  $k^3$ -Weighted FT-EXAFS spectra and (bottom)  $k$ -plot spectra of Sn-CTF and reference samples. (b) Representative HR-TEM image of Sn-CTF and corresponding EDX mapping images for C, N, and Sn atoms. The scale bar in all the images is 20 nm. (c) (left upper) Cross-sectional SEM image of Ni-CTF/GDE, which shows gas diffusion layer (GDL), micro-porous layer (MPL), and catalyst layer (CL), and (left bottom) schematic of cross-section of M-CTF/GDEs, and (right) structure of M-CTFs. Scale bar is 10 μm.



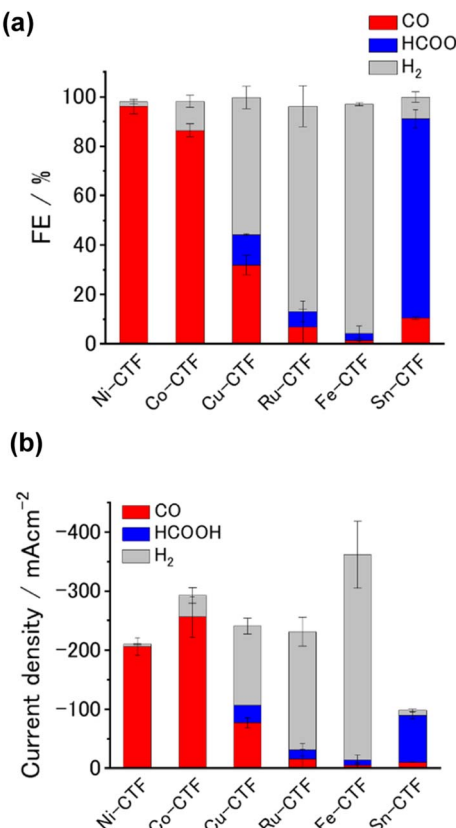


Fig. 4 (a) FE, (b) current density breakdown for products of  $\text{CO}_2$  electrolysis in the presence of M-CTFs (M = Ni, Co, Cu, Ru, Fe, Sn). Potential:  $-0.9 \text{ V}$  vs. RHE; electrolyte: 1 M  $\text{KHCO}_3$  (aq) (pH 8.6). The error bars represent the standard deviations obtained from three experimental trials.

CO production ( $\text{FE}_{\text{CO}}$ ) was greater than 98% between  $-0.5$  and  $-0.9 \text{ V}$  vs. RHE (Fig. 5(a)). Fig. 5(b) and S14<sup>†</sup> shows that the partial current density for CO generation ( $j_{\text{CO}}$ ) was maximized at  $-0.9 \text{ V}$  vs. RHE and reached  $j_{\text{CO}} = -200 \text{ mA cm}^{-2}$ . The onset potential for the competing HER was  $-0.9 \text{ V}$  vs. RHE, and the faradaic efficiency for  $\text{H}_2$  production ( $\text{FE}_{\text{H}_2}$ ) increased, accompanied by a negative potential shift. In the case of the Sn-CTF, the  $\text{FE}_{\text{HCOOH}}$  and the partial current density for formate generation with the Sn-CTF/GDE reached 85% at  $-1.0 \text{ V}$  vs. RHE and  $j_{\text{HCOOH}} = -150 \text{ mA cm}^{-2}$  at  $-1.2 \text{ V}$  vs. RHE (Fig. 5(c) and (d)). We conducted the stability tests for Sn-, Ni- and Co-CTF/GDEs. Fig. S15–S17<sup>†</sup> show that Sn-, Ni- and Co-CTF on GDE had a negligible decrease in the FE for  $\text{CO}_2\text{RR}$  for several hours. In addition, Sn- and Co-CTFs show an almost constant partial current density within this time scale. However, a 20% decrease in CO partial current density after 2 h was observed for Ni-CTF. The desorption of Ni atoms would be the main reason for the current decrease (for the detail, see Fig. S18, S19 and the caption in Fig. S16<sup>†</sup>). The appropriate choice of frameworks is required to improve stability, which is ongoing in our laboratory.

Although the adsorption strength of reaction intermediates is known to be an essential factor influencing the  $\text{CO}_2\text{RR}$ , systematic studies of the relationship between the adsorption strength and experimental activity under high-current

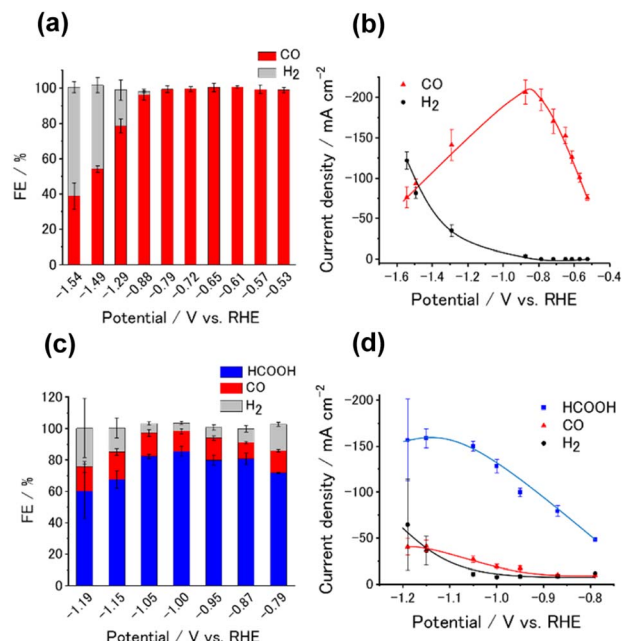


Fig. 5 Potential dependence of (a) FE and (b) partial current density for Ni-CTF/GDE in 1 M  $\text{KHCO}_3$  (aq) (pH 8.6). Potential dependence of (c) FE and (d) partial current density for Sn-CTF/GDE in 1 M  $\text{KHCO}_3$  (aq) (pH 8.6). The error bars represent the standard deviations obtained from three experimental trials.

conditions have not been reported. Given the previously discussed theoretical and experimental results, our M-CTFs are a suitable class of electrocatalysts for investigating the relationship between the adsorption strength and experimental activity because of their wide variety of available single-metal sites with high  $\text{CO}_2\text{RR}$  activity. Thus, we here discuss the dependency of the CO generation rate on the adsorption strength of intermediates under high-rate  $\text{CO}_2\text{RR}$  conditions.

Fig. 6 and S20<sup>†</sup> show the  $j_{\text{CO}}$  at  $-0.9 \text{ V}$  vs. RHE against  $\Delta G(\text{COOH})$  and  $\Delta G(\text{CO})$ , respectively. As demonstrated in Fig. 1(c), there is a linear relationship (scaling relationships)

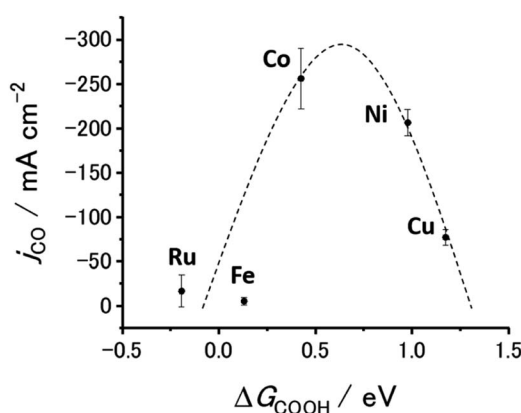


Fig. 6 Partial current density for CO generation as function of adsorption energy of COOH to M-CTFs (M = Co, Cu, Ni, Fe, Ru). Potential:  $-0.9 \text{ V}$  vs. RHE; electrolyte: 1 M  $\text{KHCO}_3$  (aq) (pH 8.6). The error bars represent the standard deviations obtained from three experimental trials.

between  $\Delta G(\text{COOH})$  and  $\Delta G(\text{CO})$ , meaning that  $\Delta G(\text{CO})$  decreases with decreasing  $\Delta G(\text{COOH})$ . Therefore, only  $\Delta G(\text{COOH})$  (or  $\Delta G(\text{CO})$ ) can serve as the descriptor for both  $\text{COOH}^*$  formation and CO desorption steps.<sup>85,86</sup> A volcano-type relation with a single peak located near the data points for the Co- and Ni-CTFs was obtained. Fig. 1(d) shows that the Co-, Fe- and Ru-CTFs bind both CO and COOH too strongly ( $>0.50$  eV), whereas the adsorption strength of these intermediates on the Sn- and Cu-CTFs was 0.37 and 0.20 eV weaker than the optimal value of  $\Delta G(\text{COOH})$ , respectively. As explained in the theoretical section, the desorption of CO and formation of COOH was the potential-determining step for M-CTFs at the lower and higher  $\Delta G$  sides, respectively. On the basis of the Sabatier principle, an appropriate binding energy for key intermediates, which is neither too strong nor too weak, leads to maximum activity.<sup>68,87</sup> As shown in Fig. 6 and S20,<sup>†</sup> a volcano-type relation was observed for the M-CTF/GDEs. These results indicate that the CO generation rate was clearly dependent on the adsorption strength of intermediates even under high-rate  $\text{CO}_2\text{RR}$  conditions. As for Co-, Fe- and Ru-CTFs,  $\Delta G(\text{COOH})$  was lower than the optimal value, meaning that CO adsorption was too strong, and its desorption became the potential determining step. By contrast,  $\text{COOH}^*$  formation became the potential-determining step for Cu-CTF with the higher  $\Delta G(\text{COOH})$ . This is the first study on the relationship between adsorption strength and high-rate  $\text{CO}_2\text{RR}$  activity.

As predicted about the selectivity between CO and HCOOH, Ni- and Co-CTFs with moderate  $\Delta G$  and Sn-CTF with high  $\Delta G$  produced CO and HCOOH, respectively (Fig. 1(c), 2 and S1<sup>†</sup>). When the adsorption of both COOH and H is weak, HCOOH formation becomes dominant, which corresponds to the reported selectivity.<sup>75,76</sup> We can also explain the selectivity between  $\text{CO}_2\text{RR}$  and HER. As previously reported and explained in the DFT parts,<sup>75,76</sup> a strong H- or COOH-adsorption is known to cause the HER selectivity against  $\text{CO}_2\text{RR}$ . Even for our M-CTFs, Fe- and Ru-CTFs exhibited stronger adsorption than others (Fig. 1(c), 2 and S1<sup>†</sup>) and showed that the HER was preferable to  $\text{CO}_2\text{RR}$ . In contrast, other M-CTFs showed that  $\text{CO}_2\text{RR}$  was dominant, which clearly corresponded to the DFT results. Thus, the product selectivity can be strongly modulated by changing the metal center, which controls the adsorption energy of the intermediate even under high-current electrolysis conditions.

These results show that the M-CTFs can be used to systematically and precisely control the adsorption energy when only the metal species is changed, even under high-rate electrolysis. The results therefore suggest that M-CTFs are an ideal platform catalyst material for high-rate electrolysis using GDEs, which is not limited to  $\text{CO}_2$  electrolysis. The M-CTFs are also expected to serve as model catalysts for establishing catalyst design guidelines specialized for high-rate electrolysis.

## Conclusions

In this study, we successfully used M-CTFs as selective and high-rate  $\text{CO}_2\text{RR}$  catalysts. The Ni- and Sn-CTFs produced CO and HCOOH on GDEs, which corresponded closely to the  $\text{CO}_2\text{RR}$

intermediate adsorption strength obtained by DFT calculations. Our results indicate that the molecular-scale design of M-CTFs can affect the  $\text{CO}_2\text{RR}$  activity with a current density greater than  $-100 \text{ mA cm}^{-2}$ . This is the first systematic study of SAECs for high-rate electrolysis of gaseous  $\text{CO}_2$ . Thus, our results provide a design direction for efficient catalysts for high-rate  $\text{CO}_2\text{RRs}$ . In addition, our M-CTFs will serve as a platform for electrocatalysts on GDEs, comparable to metal nanoparticles and metal macrocycles.

## Data availability

The data that support the findings of this study are available from the corresponding author upon reasonable request.

## Author contributions

S. N. and K. K. conceptualized the project. S. K. and T. Y. H. synthesized M-CTFs, conducted the  $\text{CO}_2\text{RR}$  performance tests, and performed the DFT calculations. S. K. and T. S. H. designed the experiment. S. K. and K. I. performed the characterization of M-CTF/GDEs and analyzed the related data. S. K., K. I. and K. K. wrote the manuscript. S. N. and K. K. co-supervised the whole project. All authors discussed the results and commented on the manuscript.

## Conflicts of interest

There are no conflicts to declare.

## Acknowledgements

This work was supported by a JSPS KAKENHI Program (grants 21J22493, 22H02175, and 20H02568) and CREST (grant JPMJCR18R3) of the Japan Science and Technology Agency. Synchrotron radiation experiments were performed using the BL01B1 beamline of SPring-8 with approval of the Japan Synchrotron Radiation Research Institute (proposals 2020A1426, 2021A1294, 2021B1204, and 2022A1165). A part of this study was supported by the Center for Integrated Nanotechnology Support, Tohoku University, sponsored by the Ministry of Education, Culture, Sport, Science and Technology, Japan (grant A-20-TU-0023). We also acknowledge Dr Y. Hayasaka and Ms S. Nakahata for the HR-TEM observation and experimental support, respectively.

## Notes and references

- 1 G. Wang, J. Chen, Y. Ding, P. Cai, L. Yi, Y. Li, C. Tu, Y. Hou, Z. Wen and L. Dai, *Chem. Soc. Rev.*, 2021, **50**, 4993–5061.
- 2 A. R. Woldu, Z. Huang, P. Zhao, L. Hu and D. Astruc, *Coord. Chem. Rev.*, 2022, **454**, 214340.
- 3 Y. Ding, J. R. Bertram, C. Eckert, R. R. Bommareddy, R. Patel, A. Conradie, S. Bryan and P. Nagpal, *J. Am. Chem. Soc.*, 2019, **141**, 10272–10282.
- 4 E. Sediva, A. J. Carrillo, C. E. Halloran and J. L. M. Rupp, *ACS Appl. Energy Mater.*, 2021, **4**, 1474–1483.



5 Y. Kuramochi, O. Ishitani and H. Ishida, *Coord. Chem. Rev.*, 2018, **373**, 333–356.

6 S. Jin, Z. Hao, K. Zhang, Z. Yan and J. Chen, *Angew. Chem., Int. Ed.*, 2021, **60**, 20627–20648.

7 A. Sacco, R. Speranza, U. Savino, J. Zeng, M. A. Farkhondehfal, A. Lamberti, A. Chiodoni and C. F. Pirri, *ACS Sustainable Chem. Eng.*, 2020, **8**, 7563–7568.

8 D. R. Kauffman, J. Thakkar, R. Siva, C. Matranga, P. R. Ohodnicki, C. Zeng and R. Jin, *ACS Appl. Mater. Interfaces*, 2015, **7**, 15626–15632.

9 M. Kö, J. Vaes, E. Klemm and D. Pant, *iScience*, 2019, **19**, 135–160.

10 H. Rabiee, L. Ge, X. Zhang, S. Hu, M. Li and Z. Yuan, *Energy Environ. Sci.*, 2021, **14**, 1959–2008.

11 S. Kato, K. Iwase, T. Harada, S. Nakanishi and K. Kamiya, *ACS Appl. Mater. Interfaces*, 2020, **12**, 29376–29382.

12 H. Yang, Q. Lin, C. Zhang, X. Yu, Z. Cheng, G. Li, Q. Hu, X. Ren, Q. Zhang, J. Liu and C. He, *Nat. Commun.*, 2020, **11**, 593.

13 K. Pellumbi, M. Smialkowski, D. Siegmund and U. P. Apfel, *Chem. - Eur. J.*, 2020, **26**, 9938–9944.

14 A. Gawel, T. Jaster, D. Siegmund, J. Holzmann, H. Lohmann, E. Klemm and U. P. Apfel, *iScience*, 2022, **25**, 104011.

15 S. Ren, D. Joulié, D. Salvatore, K. Torbensen, M. Wang, M. Robert and C. P. Berlinguette, *Science*, 2019, **365**, 367–369.

16 A. Reyes, R. P. Jansonius, B. A. W. Mowbray, Y. Cao, D. G. Wheeler, J. Chau, D. J. Dvorak and C. P. Berlinguette, *ACS Energy Lett.*, 2020, **5**, 1612–1618.

17 A. Löwe, M. Schmidt, F. Bienen, D. Kopljær, N. Wagner and E. Klemm, *ACS Sustainable Chem. Eng.*, 2021, **9**, 4213–4223.

18 A. Löwe, C. Rieg, T. Hierlemann, N. Salas, D. Kopljær, N. Wagner and E. Klemm, *ChemElectroChem*, 2019, **6**, 4497–4506.

19 M. C. O. Monteiro, S. Dieckhöfer, T. Bobrowski, T. Quast, D. Pavesi, M. T. M. Koper and W. Schuhmann, *Chem. Sci.*, 2021, **12**, 15682–15690.

20 J. R. C. Junqueira, P. B. O'Mara, P. Wilde, S. Dieckhöfer, T. M. Benedetti, C. Andronescu, R. D. Tilley, J. J. Gooding and W. Schuhmann, *ChemElectroChem*, 2021, **8**, 4848–4853.

21 P. Wilde, P. B. O'Mara, J. R. C. Junqueira, T. Tarnev, T. M. Benedetti, C. Andronescu, Y. T. Chen, R. D. Tilley, W. Schuhmann and J. J. Gooding, *Chem. Sci.*, 2021, **12**, 4028–4033.

22 C. T. Dinh, F. P. García De Arquer, D. Sinton and E. H. Sargent, *ACS Energy Lett.*, 2018, **3**, 2835–2840.

23 C. M. Gabardo, A. Seifitokaldani, J. P. Edwards, C. T. Dinh, T. Burdyny, M. G. Kibria, C. P. O'Brien, E. H. Sargent and D. Sinton, *Energy Environ. Sci.*, 2018, **11**, 2531–2539.

24 B. Endrődi, E. Kecsenovity, A. Samu, T. Halmágyi, S. Rojas-Carbonell, L. Wang, Y. Yan and C. Janáky, *Energy Environ. Sci.*, 2020, **13**, 4098–4105.

25 B. Endrődi, A. Samu, E. Kecsenovity, T. Halmágyi, D. Sebők and C. Janáky, *Nat. Energy*, 2021, **6**, 439–448.

26 B. Endrődi, E. Kecsenovity, A. Samu, F. Darvas, R. v. Jones, V. Török, A. Danyi and C. Janáky, *ACS Energy Lett.*, 2019, **4**, 1770–1777.

27 B. Endrődi, G. Bencsik, F. Darvas, R. Jones, K. Rajeshwar and C. Janáky, *Prog. Energy Combust. Sci.*, 2017, **62**, 133–154.

28 N. T. Nesbitt, T. Burdyny, H. Simonson, D. Salvatore, D. Bohra, R. Kas and W. A. Smith, *ACS Catal.*, 2020, **10**, 14093–14106.

29 F. Pelayo García de Arquer, C.-T. Dinh, A. Ozden, J. Wicks, C. McCallum, A. R. Kirmani, D.-H. Nam, C. Gabardo, A. Seifitokaldani, X. Wang, Y. C. Li, F. Li, J. Edwards, L. J. Richter, S. J. Thorpe, D. Sinton and E. H. Sargent, *Science*, 2020, **367**, 661–666.

30 M. de Jesus Gálvez-Vázquez, P. Moreno-García, H. Xu, Y. Hou, H. Hu, I. Z. Montiel, A. v. Rudnev, S. Alinejad, V. Grozovski, B. J. Wiley, M. Arenz, P. Broekmann and P. Moreno-García, *ACS Catal.*, 2020, **10**, 13096–13108.

31 T. Sau and A. Rogach, *Adv. Mater.*, 2010, **22**, 1781–1804.

32 S. Panigrahi, S. Kundu, K. Ghosh, S. Nath and S. Pal, *J. Nanopart. Res.*, 2004, **6**, 411–414.

33 G. Oskam, *J. Solgel Sci. Technol.*, 2006, **37**, 161–164.

34 P. Goulet and R. Lennox, *J. Am. Chem. Soc.*, 2010, **132**, 9582–9584.

35 K. An and G. Somorjai, *ChemCatChem*, 2012, **10**, 1512–1524.

36 A. Loiudice, P. Lobaccaro, E. Kamali, T. Thao, B. Huang, J. Ager and R. Buonsanti, *Angew. Chem., Int. Ed.*, 2016, **55**, 5789–5792.

37 M. Ma, K. Djanashvili and W. Smith, *Angew. Chem., Int. Ed.*, 2016, **55**, 6680–6684.

38 T. Zhang, X. Han, H. Yang, A. Han, E. Hu, Y. Li, X. Yang, L. Wang, J. Liu and B. Liu, *Angew. Chem., Int. Ed.*, 2020, **59**, 12055–12061.

39 S. Liu, H. Yang, S. Hung, J. Ding, W. Cai, L. Liu, J. Gao, X. Li, X. Ren, Z. Kuang, Y. Huang, T. Zhang and B. Liu, *Angew. Chem., Int. Ed.*, 2020, **59**, 798–803.

40 X. Li, H. Rong, J. Zhang, D. Wang and Y. Li, *Nano Res.*, 2020, **13**, 1842–1855.

41 Z. Liang, W. Guo, R. Zhao, T. Qiu, H. Tabassum and R. Zou, *Nano Energy*, 2019, **64**, 103917.

42 P. Kuhn, M. Antonietti and A. Thomas, *Angew. Chem., Int. Ed.*, 2008, **47**, 3450–3453.

43 P. Kuhn, A. Thomas and M. Antonietti, *Macromolecules*, 2009, **42**, 319–326.

44 R. Kamai, K. Kamiya, K. Hashimoto and S. Nakanishi, *Angew. Chem., Int. Ed.*, 2016, **55**, 13184–13188.

45 K. Iwase, T. Yoshioka, S. Nakanishi, K. Hashimoto and K. Kamiya, *Angew. Chem., Int. Ed.*, 2015, **54**, 11068–11072.

46 K. Kamiya, R. Kamai, K. Hashimoto and S. Nakanishi, *Nat. Commun.*, 2014, **5**, 5040.

47 K. Kamiya, *Chem. Sci.*, 2020, **11**, 8339–8349.

48 P. Su, K. Iwase, T. Harada, K. Kamiya and S. Nakanishi, *Chem. Sci.*, 2018, **9**, 3941–3947.

49 Y. Wang, J. Chen, G. Wang, Y. Li and Z. Wen, *Angew. Chem., Int. Ed.*, 2018, **130**, 13304–13308.

50 C. Lu, J. Yang, S. Wei, S. Bi, Y. Xia, M. Chen, Y. Hou, M. Qiu, C. Yuan, Y. Su, F. Zhang, H. Liang and X. Zhuang, *Adv. Funct. Mater.*, 2019, **29**, 1806884.

51 D. Huang, Q. Wang, W. Dong, L. Liao, H. Chen and J. Ye, *Energy Fuels*, 2022, **36**, 11601–11608.



52 L. Gong, X. Wang, T. Zheng, J. Liu, J. Wang, Y. C. Yang, J. Zhang, X. Han, L. Zhang and Z. Xia, *J. Mater. Chem. A*, 2021, **9**, 3555–3566.

53 A. M. Patel, S. Ringe, S. Siahrostami, M. Bajdich, J. K. Nørskov and A. R. Kulkarni, *J. Phys. Chem. C*, 2018, **122**, 29307–29318.

54 F. Zhou, X. Song, C. Hao and J. Qiu, *ACS Appl. Energy Mater.*, 2022, **5**, 825–831.

55 J. Artz, *ChemCatChem*, 2018, **10**, 1753–1771.

56 K. Ohashi, K. Iwase, T. Harada, S. Nakanishi and K. Kamiya, *J. Phys. Chem. C*, 2021, **125**, 10983–10990.

57 K. Iwase, S. Nakanishi, M. Miyayama and K. Kamiya, *ACS Appl. Energy Mater.*, 2020, **3**, 1644–1652.

58 X. Wei, S. Xiao, R. Wu, Z. Zhu, L. Zhao, Z. Li, J. Wang, J. S. Chen and Z. Wei, *Appl. Catal., B*, 2022, **302**, 120861.

59 X. Li, S. Xi, L. Sun, S. Dou, Z. Huang, T. Su and X. Wang, *Adv. Sci.*, 2020, **7**, 2001545.

60 F. Calle-Vallejo, J. I. Martinez, J. M. Garcia-Lastra, J. Rossmeisl and M. T. M. Koper, *Phys. Rev. Lett.*, 2012, **108**, 116103.

61 J. Rossmeisl, A. Logadottir and J. K. Nørskov, *Chem. Phys.*, 2005, **319**, 178–184.

62 F. Abild-Pedersen, J. Greeley, F. Studt, J. Rossmeisl, T. R. Munter, P. G. Moses, E. Skúlason, T. Bligaard and J. K. Nørskov, *Phys. Rev. Lett.*, 2007, **99**, 016105.

63 V. Tripkovic, M. Vanin, M. Karamad, M. E. Björketun, K. W. Jacobsen, K. S. Thygesen and J. Rossmeisl, *J. Phys. Chem. C*, 2013, **117**, 9187–9195.

64 C. Shi, H. A. Hansen, A. C. Lausche and J. K. Nørskov, *Phys. Chem. Chem. Phys.*, 2014, **16**, 4720–4727.

65 A. A. Peterson and J. K. Nørskov, *J. Phys. Chem. Lett.*, 2012, **3**, 251–258.

66 K. Chan, C. Tsai, H. A. Hansen and J. K. Nørskov, *ChemCatChem*, 2014, **6**, 1899–1905.

67 M. Anand and J. K. Nørskov, *ACS Catal.*, 2020, **10**, 336–345.

68 A. J. Medford, A. Vojvodic, J. S. Hummelshøj, J. Voss, F. Abild-Pedersen, F. Studt, T. Bligaard, A. Nilsson and J. K. Nørskov, *J. Catal.*, 2015, **328**, 36–42.

69 B. Hammer and J. K. Nørskov, *Nature*, 1995, **376**, 238–240.

70 J. K. Nørskov, F. Abild-Pedersen, F. Studt and T. Bligaard, *Proc. Natl. Acad. Sci. U. S. A.*, 2011, **108**, 937–943.

71 H. Huang, H. Jia, Z. Liu, P. Gao, J. Zhao, Z. Luo, J. Yang and J. Zeng, *Angew. Chem., Int. Ed.*, 2017, **56**, 3594–3598.

72 A. Bagger, W. Ju, A. S. Varela, P. Strasser and J. Rossmeisl, *Catal. Today*, 2017, **288**, 74–78.

73 V. Tripkovic, M. Vanin, M. Karamad, M. E. Björketun, K. W. Jacobsen, K. S. Thygesen and J. Rossmeisl, *J. Phys. Chem. C*, 2013, **117**, 9187–9195.

74 M. J. Cheng, Y. Kwon, M. Head-Gordon and A. T. Bell, *J. Phys. Chem. C*, 2015, **119**, 21345–21352.

75 A. Bagger, W. Ju, A. S. Varela, P. Strasser and J. Rossmeisl, *ChemPhysChem*, 2017, **18**, 3266–3273.

76 J. Hussain, H. Jónsson and E. Skúlason, *ACS Catal.*, 2018, **8**, 5240–5249.

77 J. S. Yoo, R. Christensen, T. Vegge, J. K. Nørskov and F. Studt, *ChemSusChem*, 2016, **9**, 358–363.

78 W. J. Durand, A. A. Peterson, F. Studt, F. Abild-Pedersen and J. K. Nørskov, *Surf. Sci.*, 2011, **605**, 1354–1359.

79 N. Han, P. Ding, L. He, Y. Li and Y. Li, *Adv. Energy Mater.*, 2020, **10**, 1902338.

80 J. T. Feaster, C. Shi, E. R. Cave, T. Hatsukade, D. N. Abram, K. P. Kuhl, C. Hahn, J. K. Nørskov and T. F. Jaramillo, *ACS Catal.*, 2017, **7**, 4822–4827.

81 M. J. Cheng, Y. Kwon, M. Head-Gordon and A. T. Bell, *J. Phys. Chem. C*, 2015, **119**, 21345–21352.

82 S. Back, J. Lim, N. Y. Kim, Y. H. Kim and Y. Jung, *Chem. Sci.*, 2017, **8**, 1090–1096.

83 Y. Wu, K. Kamiya, T. Hashimoto, R. Sugimoto, T. Harada, K. Fujii and S. Nakanishi, *Electrochemistry*, 2020, **88**, 359–364.

84 D. Barreca, S. Garon, E. Tondello and P. Zanella, *Surf. Sci. Spectra*, 2000, **7**, 81–85.

85 A. A. Peterson and J. K. Nørskov, *J. Phys. Chem. Lett.*, 2012, **3**, 251–258.

86 C. Shi, H. A. Hansen, A. C. Lausche and J. K. Nørskov, *Phys. Chem. Chem. Phys.*, 2014, **16**, 4720–4727.

87 M. Che, *Catal. Today*, 2013, **218–219**, 162–171.

